

**Microstructure, phase composition and hardness evolution in 316L stainless steel
processed by high-pressure torsion**

Jenő Gubicza^{a,*}, Moustafa El-Tahawy^a, Yi Huang^b, Hyelim Choi^c, Heeman Choe^c,

János L. Lábár^d and Terence G. Langdon^b

^aDepartment of Materials Physics, Eötvös Loránd University, Budapest, P.O.B. 32, H-1518, Hungary

^bMaterials Research Group, Faculty of Engineering and the Environment, University of Southampton, Southampton SO17 1BJ, UK

^cSchool of Advanced Materials Engineering, Kookmin University, 77 Jeongneung-ro, Seongbuk-gu, Seoul 136-702, Republic of Korea

^dInstitute for Technical Physics and Materials Science, Centre for Energy Research, Hungarian Academy of Sciences, Budapest, Hungary

*Corresponding author: Tel: +36-1-372-2876, Fax: +36-1-372-2811,
e-mail: jeno.gubicza@ttk.elte.hu

Abstract

A 316L stainless steel was processed by high-pressure torsion (HPT) to evaluate the grain refinement and phase transformation. The initial material was essentially a single phase γ -austenite with a coarse-grained microstructure of $\sim 42 \mu\text{m}$ but the grain size was reduced to $\sim 45 \text{ nm}$ after 10 turns of HPT. In addition, there was a phase transformation and the initial γ -austenite transformed initially to ε -martensite and finally to α' -martensite with increasing strain. The dislocation density increased to an exceptionally high value, of the order of $\sim 10^{16} \text{ m}^{-2}$, in the main α' -martensite phase after 10 HPT revolutions. The formation of the multiphase nanocrystalline microstructure yielded a four-fold increase in hardness to reach an ultimate value of $\sim 6000 \text{ MPa}$. The Hall-Petch behavior of the HPT-processed alloy is compared directly with coarse-grained materials.

Keywords: grain refinement, hardness, nanostructured materials, phase transformation, steel

1. Introduction

The 316L stainless steel is often used as a material for orthopaedic implants [1]. The three main alloying elements in 316L steel are Cr, Ni and Mo where Cr is added to suppress atmospheric corrosion (i.e. rusting) and Ni and Mo increase the corrosion resistance of the alloy against chloride-containing human body fluids. The alloy designation includes the letter L to indicate a low carbon content (<0.03 wt.%) which also improves the corrosion resistance. The 316L steel is also used as a structural material in nuclear power plants owing to its high strength, good ductility, high fracture toughness, excellent corrosion resistance and low absorption rate of neutron radiation [2-4]. The addition of Ni stabilizes the metastable face-centred cubic (fcc) structure at room temperature and this is designated γ -austenite [1]. The fcc iron crystal is more ductile than the usual body-centred cubic (bcc) structure of iron thereby producing a high toughness. As a result, the maximum tensile elongation for coarse-grained 316L steel can reach 84%. At the same time, the hardness and the ultimate tensile strength values in 316L steel are relatively low, of the order of ~1400 MPa and ~590 MPa, respectively, compared to steels having a bcc structure [5].

In all applications of 316L steel the mechanical strength is an important factor. Over the last two decades, severe plastic deformation (SPD) was successfully applied for improving the hardness of metallic materials [6-8] and, among all SPD procedures, high-pressure torsion (HPT) is generally considered the most effective technique for producing grain refinement and ultrafine-grained (UFG) or nanocrystalline microstructures [9].

The influence of HPT on the mechanical performance of 316L steel was studied recently [5] and it was found that ten turns of HPT at room temperature gave an increase in hardness from 1400 MPa to 4900 MPa and a decrease in the elongation to failure from 84% to 23% while the material remained fully fcc γ -austenite [5]. Additional annealing at 500°C for 1 h yielded further hardening to 5600 MPa with a simultaneous reduction of elongation to 16%,

where this hardening was explained by the development of subgrain/grain boundaries from the dislocations formed during HPT. Other studies showed that γ -austenite in 316L steel may transform partially into bcc α' -martensite during HPT [10]. However, charging of the samples with 22.3 ppm hydrogen reduced the fraction of the transformed α' -martensite from 50% to 10%. This effect is explained by the slip localization due to hydrogen-enhanced slip planarity which then reduces the possibility of a strain-induced transformation of metastable γ -austenite to α' -martensite.

The temperature of the HPT processing strongly influences the phase composition, the microstructure and the mechanical performance of 316L steel. If HPT is conducted at very low temperatures, between -196 and 20 °C, γ -austenite transforms into hexagonal close-packed (hcp) ϵ -martensite [11]. At high HPT temperatures (>450 °C), dislocation glide is the dominant deformation mechanism in γ -austenite. At medium deformation temperatures, between 20 and 450 °C, twinning was also observed. Both twinning and the development of ϵ -martensite is attributed to the low stacking fault energy (SFE) of 316L steel. The hcp ϵ -martensite can be formed if stacking faults are developed on every second $\{111\}$ plane in fcc γ -austenite. At HPT-processing temperatures between -196 and 720 °C, α' -martensite was not observed [11]. Due to the change of the deformation mechanisms in 316L steel, an abnormal hardening was observed with increasing HPT temperature. Thus, the highest strength was detected at ~ 600 °C while at lower and higher temperatures the hardness decreased. Although numerous investigations were performed on 316L steel, there has been no detailed study of the concomitant grain refinement and phase transformation in HPT-processed 316L steel as a function of the number of turns imposed in the HPT processing.

The present investigation was designed to address this deficiency by examining the evolution of the phase composition, the grain size and the dislocation density during HPT processing of 316L stainless steel. The study of the strain-induced phase transformation in

HPT-processed 316L steel is particularly important in the hydrogen embrittlement of 316L steel because the insight gained from this investigation can apply directly to studies where the hydrogen influence is dependent upon the type of phases present during any mechanical deformation process [4]. In addition, scanning and transmission electron microscopy were used to examine the microstructures on cross-sections of the as-processed disks as a function of the numbers of HPT revolutions. By contrast, earlier studies examined only the disk surfaces of 316L steel after HPT processing [5,10,11]. In addition, the dislocation densities at the peripheries of the disks were determined by X-ray line profile analysis to provide the first information on dislocation densities in 316L stainless steel processed by HPT. The evolution of hardness during HPT and its relation to grain size was also investigated.

2. Experimental material and procedures

The chemical composition of the 316L stainless steel samples is shown in Table 1. The material was annealed at 1100°C for 1 h and then quenched to room temperature in water to give a coarse-grained single phase γ -austenite. For HPT processing, disks were prepared with diameters of 9.85 mm and thicknesses of ~0.85 mm. All disks were processed by HPT operating under quasi-constrained conditions [12,13] with an applied pressure of 6.0 GPa at room temperature. The HPT deformation was continued for various numbers of revolutions, N , from $\frac{1}{4}$ to 10 turns.

The HPT-processed microstructures were studied on the cross-sections of the disks using an FEI Quanta 3D scanning electron microscope (SEM). Each surface was mechanically polished with 1200, 2500 and 4000 grit SiC abrasive papers and then the polishing was continued with a colloidal silica suspension (OP-S) with a particle size of 40 nm. Finally, the surface was electropolished at 28 V and 0.5 A using an electrolyte with a composition of 70% ethanol, 20% glycerine and 10% perchloric acid (in vol.%). The electron

backscattered diffraction (EBSD) images were taken with a step size of 30 nm and evaluated using OIM software (TexSem Laboratories).

In the periphery of the HPT-processed disks it was not possible to investigate the strongly refined and distorted microstructure by EBSD. Therefore, transmission electron microscopy (TEM) investigations were applied for the determination of grain size. The TEM lamellae were prepared with special care from the cross-sections of the disks in order to avoid additional unwanted annealing of the samples. Low temperature glue (GATAN G1) was used at 60°C to fix the sample in the 3 mm diameter Ti disk. Ion milling was conducted at 7 keV with continuous cooling of the sample by liquid nitrogen. The TEM examinations were performed in a Philips CM20 electron microscope operating at 200 keV. Images and diffraction patterns were recorded on imaging plates and the diffraction patterns were indexed using the ProcessDiffraction program [14,15].

The phase composition, the crystallite size and the dislocation density were investigated by X-ray diffraction (XRD). The XRD patterns were measured using a high-resolution diffractometer with $\text{CoK}_{\alpha 1}$ radiation (wavelength: $\lambda = 0.1789$ nm). The X-ray line profile analysis (XLPA) was carried out with the Convolutional Multiple Whole Profile (CMWP) fitting method [16]. In this procedure, the diffraction pattern is fitted by the sum of a background spline and the convolution of the instrumental pattern and the theoretical line profiles related to the crystallite size and dislocations. Because of the nanocrystalline microstructures of the samples, the physical broadening of the profiles was much larger than the instrumental broadening and therefore instrumental correction was not applied in the evaluation. The theoretical profile functions used in this fitting procedure were calculated on the basis of a model of the microstructure where the crystallites have spherical shape and a log-normal size distribution. The following parameters of the microstructure were determined from the CMWP fitting procedure: the area-weighted mean crystallite size ($\langle x \rangle_{\text{area}}$) and the

mean dislocation density (ρ). The value of $\langle x \rangle_{\text{area}}$ was calculated as $\langle x \rangle_{\text{area}} = m \exp(2.5 \sigma^2)$, where m is the median and σ^2 is the log-normal variance of the crystallite size distribution.

The hardness was measured as a function of the distance from the centre of the HPT-processed disks using a Zwick Roell ZH μ hardness tester with a Vickers indenter, an applied load of 500 g and a dwell time of 10 s. Additional nanohardness measurements were performed on the cross-sections of the disks using a UMIS nanohardness device with a Vickers indenter and a maximum load of 3 mN. The size of the indents was $\sim 1 \mu\text{m}$. A series of 400 indentations was recorded which were arranged in an 8×50 matrix with lateral spacings of $10 \mu\text{m}$. The shorter edge of this matrix was parallel to the disk diameter.

3. Experimental results

3.1. Change of phase composition during HPT

The microstructure of the initial material is illustrated in Fig. 1. The EBSD images in Figs. 1a and b show the grain structure in fcc γ -austenite and bcc α' -martensite, respectively. It is apparent that the majority (~ 97 vol.%) of the initial sample is γ -austenite with a mean grain size of $\sim 42 \mu\text{m}$. Smaller α' -martensite grains are also observed besides the austenite grains as shown in Fig. 1b. Figs. 2a and b present the X-ray diffractograms obtained for the centre and the periphery of the disks, respectively, in the initial specimen and the HPT-processed samples with the smallest ($N = 1/4$) and the highest ($N = 10$) numbers of turns. The comparison of these diffraction patterns reveals a change of the phase composition due to HPT straining. The initial sample is almost a single phase γ -austenite with a very small fraction of α' -martensite in accordance with the EBSD results. Processing by HPT gave a phase transformation such that fcc γ -austenite transformed into hcp ϵ - and bcc α' -martensites. The higher the numbers of turns and the greater the distance from centre, the more advanced the transformation. For the highest number of turns ($N = 10$) the HPT-processed disk at the

periphery contains mainly α' -martensite. This observation suggests that the phase transformation is promoted by the strain applied in the HPT processing.

3.2. Microstructure evolution as determined by SEM and EBSD

Backscattered electron images were taken on the cross-sections of the initial and the HPT-processed samples by SEM. Figure 3 shows representative SEM images for the initial sample and the disks processed by ¼ and 10 turns of HPT in order to illustrate the evolution of the cross-sectional microstructure. The initial specimen exhibits a uniform coarse-grained microstructure but the strain gradient along the radius of the HPT-processed disk causes a non-uniform microstructure: in the centre (low strain) coarse grains of several tens of microns were detected while far from the centre (large strain) a flow pattern was developed which consists of dark and bright regions in the SEM images. The coarse-grained microstructure in the centre and the flow pattern at the periphery for the sample processed by ¼ turn are shown at higher magnifications in Figs. 4a and b, respectively. The grain size was not refined to the UFG regime in the vicinity of the disk centre (closer than 0.5 mm to the centre) even after 5 turns. At the same time, apart from the centre region the grain size cannot be resolved in the SEM images due to the very fine and distorted microstructure. After HPT for 10 turns, the grain size cannot be determined by SEM even in the centre. In addition to the grain refinement, cracks developed in the samples processed by three or more turns as revealed by the SEM images in Figs. 4c and d taken on the cross-sections of disks processed by 3 and 10 turns, respectively.

In the centre of the HPT-processed disks, lamellae were formed inside the coarse grains which appear in bright contrast in the SEM images (see, for example, Fig. 4a for ¼ turn). Figure 5a shows these lamellae at a higher magnification. The image quality (IQ) map in Fig. 5b reveals low IQ values in the bright regions suggesting severely distorted microstructures in these volumes. The EBSD images in Figs. 5c-e show that in most of the

bright regions the fcc γ -austenite transformed into ϵ -martensite with hcp crystal structure. It has been shown [17] that ϵ -martensite can be formed by developing stacking faults (SFs) on every second $\{111\}$ plane in fcc γ -austenite. The IQ values are low in all ϵ -martensite lamellae, indicating severe distortion in this phase which may be caused by dislocations and SFs in the hexagonal structure. If the sequence of SFs does not follow the order required for hcp stacking, the IQ values are low but ϵ -martensite is not identified. Such bands can be seen in the middle and the right side in Fig. 5b. Therefore, it can be concluded that the areas with bright contrast in the SEM images are ϵ -martensite lamellae or severely deformed bands. Fig. 5e shows that α' -martensite grains were nucleated in the ϵ -martensite bands. These grains are less distorted as indicated by the higher IQ values (see Fig. 5b) and have darker contrast in the SEM image compared to ϵ -martensite (see Fig. 5a). The observed contrast difference between ϵ - and α' -martensites is consistent with earlier investigations [17,18]. The present SEM/EBSD investigations suggest the sequence $\gamma \rightarrow \epsilon \rightarrow \alpha'$ for the phase transformation during HPT-processing, which is in accordance with results reported for other deformation methods [17,19-21]. The fractions of ϵ - and α' -martensites increased at the expense of γ -austenite with increasing number of HPT turns as illustrated by the EBSD images in Fig. 6 taken at the centre of the disk processed by $\frac{1}{2}$ turn. This observation is in accordance with the XRD experiments shown in Fig. 2.

The SEM images revealed flow patterns with bright and dark regions on the cross-sections apart from the sample centre for all HPT-processed disks. This flow pattern is illustrated for $\frac{1}{4}$ turn in Fig. 4b. The thickness of the bright and dark regions varies between 2 and 20 μm independently of their positions along the disk radius. Energy-dispersive X-ray spectroscopy (EDS) in SEM revealed no significant difference between the chemical compositions of these two regions. Additional EBSD investigations, which are not shown here, indicated that all three crystalline phases existed in both regions. However, in the bright

volumes the ratio of the fractions of ϵ - and α' -martensite is much larger than in the dark volumes. As an example, after $\frac{1}{4}$ turn the fractions of the γ , ϵ and α' phases in the two neighbouring bright and dark regions were determined as 13%, 62%, 25% and 4%, 42%, 54%, respectively. As the contrast of ϵ -martensite in the SEM images is brighter than for γ -austenite or α' -martensite (see Figs. 5 and 6), the larger fraction of ϵ -martensite yields brighter contrast in the flow pattern.

The mechanical performance of the areas with dark and bright contrast were determined by nanoindentation. In order to ensure that the indent size was below the thickness of the dark and bright regions, measured between ~ 2 and ~ 10 μm as determined from SEM images as for the $\frac{1}{4}$ turn in Fig. 4b, the load was limited to 3 mN to give an indent size below 1 μm . The mean and the standard deviation of the nanohardness values for the bright region were obtained as 9.0 and 1.2 GPa, respectively, and the corresponding values for the dark region were 9.9 and 1.4 GPa, respectively. This means the hardness values are very close in these two regions despite their different phase compositions. Apart from the centre part of the disks, the grain size was of the order of the pixel size of the EBSD investigation (~ 30 nm) and the microstructure was very distorted so that it was not possible to determine the grain size using EBSD. Thus, TEM was performed to study the grain size far from the disk centre.

3.3. Grain size and dislocation density by TEM and XLPA

Close to the periphery of the HPT-processed disks, the microstructure was studied by TEM. The dark field TEM image in Fig. 7a shows that the grain structure is very fine at the periphery even after $\frac{1}{4}$ turn of HPT. The grain size was determined from the dark-field TEM images as the diameter of the individual grains. About one hundred grains were evaluated for each disk. The average grain size was measured as ~ 120 nm for this sample. The grain size was further refined with increasing numbers of HPT revolutions as shown in Fig. 8.

Representative TEM images obtained at the periphery after ½ and 10 turns are shown in Figs 7b and c, respectively. After 10 turns the average grain size was reduced to ~45 nm at the periphery of the HPT-processed disk. The different crystalline phases were not separated in the TEM images and therefore the grain sizes plotted in Fig. 8 represent the average values for all phases in the peripheral regions of the disks. As noted in section 3.2, after 10 turns coarse grains were not observed at the disk centre by SEM and therefore this microstructure was also investigated by TEM (see Fig. 7d). The measured average grain size was ~95 nm thereby demonstrating the occurrence of a nanocrystalline microstructure even in the centre of the sample processed by 10 revolutions of HPT.

The XLPA was applied to determine the crystallite size and the dislocation density in the HPT-processed samples. Due to the strongly overlapping peaks of γ -austenite and ε -martensite (see Fig. 2), the line profiles of these phases were not evaluated. Therefore, the parameters of the microstructure were determined only for α' -martensite. A major attempt was undertaken to determine crystallite size and dislocation density values characterizing relatively large volumes in the samples and accordingly the XRD patterns were evaluated only in the peripheral regions of the disks where α' -martensite was the major phase. As an example, Fig. 8 illustrates the fitting on the XRD pattern taken at the periphery of the disk processed by 10 turns of HPT. Four peaks of α' -martensite were measured by Co radiation in the Bragg angle range 40-140°. These reflections were fitted by the CMWP method as indicated by the indices of reflections in Fig. 8. The peaks of γ -austenite and ε -martensite phases were put into the background. The difference between the measured and the fitted diffractograms is practically zero as shown at the bottom of Fig. 8, indicating an excellent fitting of the theoretical pattern to the measured diffractogram. Therefore, the reliability of the values of the microstructural parameters (crystallite size and dislocation density) is high despite the overlapping of the peaks of the different phases. The uncertainty of the results was

determined from the error of the fitted parameters as given by the CMWP software. The uncertainties of the crystallite size and the dislocation density were in the range 5-15%. In addition, each fitting procedure was repeated several times using considerably different initial parameter values. The difference between the results obtained by the repeated fitting procedures was below their errors given by the CMWP program.

Figure 9 shows the average crystallite size and dislocation density as a function of the number of HPT revolutions. It was found that the crystallite size decreased from ~37 to ~21 nm while the dislocation density increased from $\sim 66 \times 10^{14} \text{ m}^{-2}$ to $\sim 133 \times 10^{14} \text{ m}^{-2}$ with increasing numbers of HPT turns from $\frac{1}{4}$ to 10. It is therefore concluded that the crystallite size is very small and the dislocation density is very large at the peripheries of the disks even after $\frac{1}{4}$ turn. After 10 revolutions, the crystallite size and dislocation density reached, respectively, exceptionally small (~21 nm) and large ($\sim 133 \times 10^{14} \text{ m}^{-2}$) values. It is noted that this crystallite size is smaller than the grain size obtained by TEM by a factor of ~2-4. This apparent discrepancy is often observed in SPD-processed materials and is readily explained by the breaking of X-ray coherency due to the small misorientations inside the grains [22]. Therefore, the XLPA measures the size of the subgrains or dislocation cells rather than the true grain size. The better statistics of XLPA compared to TEM may also contribute to the difference between the crystallite size and the grain size values. For each sample, about one hundred grains were evaluated in the TEM images while the number of crystallites contributing to the X-ray diffraction peaks was at least three orders of magnitude larger.

3.4. Evolution of hardness in the HPT-processed stainless steel

Figure 10 shows the microhardness as a function of the distance from the centre for the disks processed for different numbers of HPT turns. The hardness of the initial material was ~1400 MPa throughout the disk. After $\frac{1}{4}$ revolution there was a strong hardening and the hardness values increased by factors of ~2.7 and ~3.5 in the centre and periphery,

respectively. A further increase in the numbers of turns gave additional hardening and the highest hardness of ~6000 MPa was achieved at the periphery of the disk processed by 10 revolutions. It is noted that this value is more than 4 times larger than the hardness of the initial material. Furthermore, the results show that most of this increment in hardness was achieved after only $\frac{1}{4}$ turn of HPT. The microhardness increased with distance from the centre for all disks in accordance with the increase of strain along the HPT sample radius. This increasing hardness with increasing distance from the centres of the disks is consistent with the general trends reported for many metals processed by HPT [23]. Furthermore, the hardness distribution remained inhomogeneous even after 10 revolutions of HPT indicating that a saturation in hardness was not achieved in the disk centre after the highest number of turns. A failure to achieve a hardness saturation is consistent with other recent results from HPT processing where there was no saturation in a NiTi alloy after 40 turns [24] or in a β -Ti alloy after 50 turns [25]

4. Discussion

4.1 The phase transformation and grain refinement in 316L stainless steel

The use of EBSD and XRD in this investigation showed that the initial fcc γ -austenite transformed gradually into hcp ϵ - and bcc α' -martensites during HPT (see Figs. 2, 5 and 6). The phase transformation followed the sequence $\gamma \rightarrow \epsilon \rightarrow \alpha'$. Previous studies [20,21,26] showed that the $\gamma \rightarrow \alpha'$ transformation can occur directly or with the formation of the intermediate ϵ -martensite phase. Theoretical calculations [27] suggest that ϵ -Fe is a high-pressure modification of iron and is stable only at pressures above ~10 GPa. However, this phase is often observed after deformation performed at pressures lower than 10 GPa. For example, in the present experiments a large fraction of ϵ -martensite was detected although the HPT pressure was only 6 GPa. This apparent dichotomy can be explained by the local stresses inside the material which may be higher than the external pressure. The low stacking fault

energy (SFE) in 316L steel may also facilitate the formation of ϵ -martensite. The alloying elements (e.g. Cr and Ni) in stainless steels reduce the SFE to a value lower than 20 mJ/m^2 [28] leading to an easier formation of SFs. If SFs are developed on every second $\{111\}$ plane in fcc γ -austenite, the fcc stacking ABCABC transforms into the hcp structure ABABAB. Thus, ϵ -martensite may form in the lamellae exhibiting this special order of SFs. As the SFs are formed by gliding of partial dislocations in fcc crystals, ϵ -Fe is most probably developed in deformation bands and there is evidence that α' -martensite forms at the intersection of these deformation bands. However, the present investigation suggests that α' -martensite grains may be nucleated in the ϵ -martensite lamellae even if they are not intersected by other deformation bands (see, for example, Fig. 5). It should be noted that the high fraction of α' -martensite in the present HPT-processed samples most probably deteriorates the corrosion resistance of the 316L steel since the fcc γ -austenite has better resistance against corrosion [29]. It is also noted that a reverse martensitic transformation ($\alpha' \rightarrow \epsilon$) was observed during room temperature HPT in a stainless steel with a different chemical composition [30].

The present results demonstrate that the grain refinement in 316L steel is very fast at the periphery of the HPT-processed disks and a nanocrystalline microstructure develops after only $\frac{1}{2}$ turn. At the same time, coarse grains with sizes of $\sim 30\text{-}40 \text{ }\mu\text{m}$ can be observed in the centre even after 5 turns. It should be noted, however, that these grains are fragmented into lamellae containing γ , ϵ and α' phases and therefore their strengthening effect is much larger than for the initial grains with similar sizes. The large hardening effect of this lamellae microstructure is demonstrated by the high hardness increment in the centres of the disks after $\frac{1}{4}$ turn (see Fig. 10). The very different microstructures in the centre and the periphery yield a strong hardness gradient along the disk radius which is maintained even after 10 turns of HPT. In order to achieve a more homogeneous microstructure and hardness, a larger number of HPT revolutions will be required. It should be noted, however, that cracks developed

during HPT processing (see Fig. 4) which reduce the tensile strength of the material. Thus, it is possible that further straining by HPT may lead to more extensive cracking and an overall diminution in the tensile performance of the 316L steel.

4.2 Dislocation density and the Hall-Petch relationship

The dislocation density in α' -martensite at the disk periphery was very large even after $\frac{1}{4}$ turn ($\sim 66 \times 10^{14} \text{ m}^{-2}$) and it further increased to $\sim 133 \times 10^{14} \text{ m}^{-2}$ after 10 revolutions of HPT. This value is extremely high compared to dislocation densities obtained by XLPA for other HPT-processed materials [31]. The grain size was also very small at the periphery even after $\frac{1}{4}$ turn ($\sim 120 \text{ nm}$) and this was further refined to $\sim 45 \text{ nm}$ after 10 revolutions. This nanocrystalline microstructure led to a very high hardness at the peripheries of the disks (see Fig. 10).

The correlation between the grain size, d , and the hardness, H , is usually described by the Hall-Petch relationship which is given by [32,33]

$$H = H_0 + k_H d^{-\frac{1}{2}}, \quad (1)$$

where H_0 and k_H depend on the structure and the chemical composition of the material. In addition, the values of H_0 and k_H are often different for coarse-grained and UFG (or nanocrystalline) microstructures. For example, in Cu when the grain size is reduced to the range $\sim 20\text{-}100 \text{ nm}$ the Hall-Petch slope, k_H , decreases [31]. This breakdown of Hall-Petch behavior is usually explained by the grain size dependence of the stress required to operate a Frank-Read source [34] and the strong reduction in the numbers of dislocations in pile-ups with decreasing grain size [35].

There is also a similar difference between the Hall-Petch parameters for coarse-grained and UFG regimes in 316L steel. Figure 11 shows a Hall-Petch plot for 316L steel using published data [36-41] and the results from this study. It is evident that, considering the total grain size range from 35 nm to $49 \mu\text{m}$, the data do not follow a single Hall-Petch

equation. On the contrary, separate lines may be fitted for the datum points of the coarse-grained and UFG samples. For grain sizes larger than $\sim 1 \mu\text{m}$, $H_0 = 745 \text{ MPa}$ and $k_H = 2804 \text{ MPa}\cdot\mu\text{m}^{1/2}$. For the UFG regime, the straight line in the Hall-Petch plot was determined by fitting the results obtained in this study as represented by solid circles. However, some datum points from investigations with grain sizes smaller than $\sim 1 \mu\text{m}$ also follow this trend which is given by values $H_0 = 3220 \text{ MPa}$ and $k_H = 580 \text{ MPa}\cdot\mu\text{m}^{1/2}$. The data in Fig. 11 were obtained on 316L samples with different phase compositions which are indicated in the figure legend. Thus, it can be seen that the grain size has a more deterministic effect on hardness compared with the influence of the phase composition so that datum points with similar grain sizes but different phase compositions lie close to each other in the Hall-Petch plot. By contrast, it is readily apparent that there are differences between the hardness values of the samples with similar grain sizes and different phase compositions. In most cases, a higher fraction of γ -austenite is accompanied by a slightly lower hardness for similar grain sizes and this is most probably due to the softer fcc lattice (for example, on the right side of the Hall-Petch plot in Fig. 11).

5. Summary and conclusions

1. Coarse-grained 316L stainless steel with an fcc structure (γ -austenite) and a grain size of $\sim 42 \mu\text{m}$ was processed by HPT under a pressure of 6.0 GPa for up to 10 turns. The grain size was reduced to $\sim 45 \text{ nm}$ at the disk periphery after 10 turns.

2. During HPT deformation, the fcc structure was gradually transformed into hcp and bcc phases (ϵ - and α' -martensites, respectively). The ϵ -martensite formed initially as lamellae in the γ -austenite coarse grains and then α' -martensite grains were nucleated in the ϵ -martensite phase. At very high strains in the peripheral region of the disk after 10 turns, the main phase was α' -martensite.

3. Examination of the α' -martensite by X-ray line profile analysis after 10 turns gave a crystallite or subgrain size of ~ 21 nm and an exceptionally high dislocation density of $\sim 133 \times 10^{14} \text{ m}^{-2}$.

4. Processing by HPT increased the hardness from ~ 1400 to ~ 3800 MPa in the disk centre after $\frac{1}{4}$ turn and the hardness increased with increasing numbers of revolutions and distance from the centre. A maximum hardness of ~ 6000 MPa was achieved at the periphery of the disk processed by 10 turns of HPT.

5. The grain size versus hardness results followed the Hall-Petch relationship but the slopes were different in the coarse-grained and ultrafine-grained regimes. The results show the hardness is more sensitive to the grain size than the phase composition.

Acknowledgements

This work was supported by the Hungarian Scientific Research Fund, OTKA, Grant No. K-109021 and the authors are grateful to Mr. Peter Szommer and Mr. Gabor Varga for the nanoindentation and EBSD investigations, respectively. Two of the authors were supported by the European Research Council under Grant Agreement No. 267464-SPDMETALS (YH and TGL).

References

1. G.L. Lucas, F.W. Cooke, E.A. Friis, *A primer of biomechanics*, Springer Science + Business Media, New York, NY, 1999.
2. W.G. Kim, S.N. Yin, W.S. Ryu, C.B. Lee, *J. Korean Inst. Met. Mater.* 46 (2008) 118-124.
3. I. Lee, *J. Korean Inst. Met. Mater.* 46 (2008) 357-362.
4. Y. Kim, Y. Kim, D. Kim, S. Kim, W. Nam, H. Choe, *Mater. Trans.* 52 (2011) 507-513.
5. H. Wang, I. Shuro, M. Umemoto, H.H. Kuo, Y. Todaka, *Mater. Sci. Eng. A* 556 (2012) 906-910.
6. R.Z. Valiev, Y. Estrin, Z. Horita, T.G. Langdon, M.J. Zehetbauer, Y.T. Zhu, *JOM* 58(4) (2006) 33-39.
7. T.G. Langdon, *Acta Mater.* 61 (2013) 7035-7059.
8. R.Z. Valiev, A.P. Zhilyaev, T.G. Langdon, *Bulk Nanostructured Materials: Fundamentals and Applications*, Wiley, Hoboken, NJ, 2014.
9. A.P. Zhilyaev, T.G. Langdon, *Prog. Mater. Sci.* 53 (2008) 893-979.
10. Y. Mine, Z. Horita, Y. Murakami, *Acta Mater.* 57 (2009) 2993-3002.
11. S. Scheriau, Z. Zhang, S. Kleber, R. Pippan, *Mater. Sci. Eng. A* 528 (2011) 2776-2786.
12. R.B. Figueiredo, P.R. Cetlin, T.G. Langdon, *Mater. Sci. Eng. A* 528 (2011) 8198-8204.
13. R.B. Figueiredo, P.H.R. Pereira, M.T.P. Aguilar, P.R. Cetlin, T.G. Langdon, *Acta Mater.* 60 (2012) 3190-3198.
14. J.L. Lábár, *Ultramicros.* 103 (2005) 237-249.
15. J.L. Lábár, B.P. Barna, M. Adamik, Zs. Czigány, Zs. Fogarassy, Z.E. Horváth, O. Geszti, F. Misják, J. Morgiel, G. Radnóczy, G. Sáfrán, L. Székely and T. Szüts, *Microsc. Microanal.* 18 (2012) 406-420.
16. G. Ribárik, J. Gubicza, T. Ungár, *Mater. Sci. Eng. A* 387-389 (2004) 343-347.

17. S. Martin, C. Ullrich, D. Simek, U. Martin, D. Rafaja, *J. Appl. Cryst.* 44 (2011) 779-787.
18. Y. Huang, M. Kawasaki, T.G. Langdon, *Adv. Eng. Mater.* 15 (2013) 747-755.
19. J.G. Parr, *Acta Cryst.* 5 (1952) 842-843.
20. H.M. Otte, *Acta Metall.* 5 (1957) 614-627.
21. B. Cina, *Acta Metall.* 6 (1958) 748-762.
22. T. Ungár, G. Tichy, J. Gubicza, R. J. Hellmig, *Powder Diffraction* 20 (2005) 366-375.
23. M. Kawasaki, *J. Mater. Sci.* 49 (2014) 18-34.
24. H. Shahmir, M. Nili-Ahmadabadi, Y. Huang, T.G. Langdon, *J. Mater. Sci.* 49 (2014) 2998-3009.
25. K. Sharman, P. Bazarnik, T. Brynk, A.G. Bulutsuz, M. Lewandowska, Y. Huang, T.G. Langdon, *J. Mater. Res. Tech.* 4 (2015) 79-83.
26. G. Kurdjumow, G. Sachs, *Z. Phys.* 64 (1930) 325-343.
27. M. Friák, M. Sob, *Phys. Rev. B* 77 (2008) 174117.
28. R. E. Schramm, R. P. Reed, *Metall. Trans. A* 6 (1975) 1345-1351.
29. P.D. Harvey, *Engineering Properties of Steel*, ASM, Metals Park, OH, 1982.
30. R.B. Figueiredo, F.L. Sicupira, L.R.C. Malheiros, M. Kawasaki, D.B. Santos, T.G. Langdon, *Mater. Sci. Eng. A* 625 (2015) 114-118.
31. J. Gubicza, *Defect Structure in Nanomaterials*, Woodhead Publishing, Cambridge, UK, 2012.
32. E.O. Hall, *Proc. Phys. Soc. London B* 64 (1951) 747-753.
33. N.J. Petch, *J. Iron Steel Inst.* 174 (1953) 25-28.
34. Y. Estrin, H.S. Kim, F.R.N. Nabarro, *Acta Mater.* 55 (2007) 6401-6407.
35. N.Q. Chinh, J. Gubicza, T.G. Langdon, *J. Mater. Sci.* 42 (2007) 1594-1605.
36. M. Eskandari, A. Najafizadeh, A. Kermanpur, *Mater. Sci. Eng. A* 519 (2009) 46-50.

37. M. Eskandari, A. Zarei-Hanzaki, H.R. Abedi, *Mater. Design* 45 (2013) 674-681.
38. I. Uçok, T. Ando, N.J. Grant, *Mater. Sci. Eng. A* 133 (1991) 284-287.
39. G. Marnier, C. Keller, J. Noudem, E. Hug, *Mater. Design* 63 (2014) 633-640.
40. A. Belyakov, M. Odnobokova, A. Kipelova, K. Tsuzaki, R. Kaibyshev, *IOP Conf. Series: Mater. Sci. Eng.* 63 (2014) 012156.
41. H. Wang, I. Shuro, M. Umemoto, H.-H. Kuo, Y. Todaka, *Mater. Sci. Eng. A* 556 (2012) 906-910.

Figure and table captions

Table 1: The concentrations of the main alloying elements as determined by energy-dispersive X-ray spectroscopy for 316L steel used in this study.

Fig. 1: EBSD images showing the grain structure in the initial sample for (a) fcc γ -austenite and (b) bcc α' -martensite.

Fig. 2: X-ray diffractograms obtained (a) for the centre (a) and (b) for the periphery of disks in the initial condition and after HPT processing with the smallest ($N = 1/4$) and the highest ($N = 10$) numbers of turns.

Fig. 3: Backscattered electron images obtained by SEM on the cross-sections of the initial sample and the disks processed by HPT for $1/4$ and 10 turns.

Fig. 4: SEM images of the coarse-grained microstructure in (a) the centre and (b) the flow pattern at the periphery for the sample processed by $1/4$ turn. Cracks on the cross-section of the disks processed by (c) 3 and (d) 10 turns.

Fig. 5: SEM image (a), IQ map (b), and crystallographic orientation maps of γ -austenite (c), ϵ -martensite (d) and α' -martensite (e) for the centre of the disk processed by $1/4$ turn.

Fig. 6: SEM image (a) and crystallographic orientation maps of γ -austenite (b), ϵ -martensite (c) and α' -martensite (d) for the center of the disk processed by $1/2$ turn.

Fig. 7: TEM images obtained at the periphery of the disks processed by $\frac{1}{4}$ (a), $\frac{1}{2}$ (b) and 10 (c) turns and at the centre after 10 revolutions (d).

Fig. 8: Fitting on the XRD pattern taken on the periphery of the disk processed by 10 turns of HPT. The open circles and the solid line represent the measured and the fitted patterns, respectively. The indices of reflections of the evaluated peaks of α' -martensite are given above the reflections. The difference between the measured and fitted diffractograms is shown at the bottom of the figure.

Fig. 9: The average grain size obtained by TEM and the crystallite size and dislocation density determined by X-ray line profile analysis for α' -martensite at the periphery of the HPT disks as a function of the numbers of revolutions.

Fig. 10: Microhardness as a function of the distance from the centred of disks processed for different numbers of HPT turns.

Fig. 11: Hall-Petch plot for the relationship between the Vickers hardness and the grain size, d , measured in this study (solid symbols) and in earlier reports [36-41] for 316L steel: the phase compositions are given at the symbols.

Fig. 1.

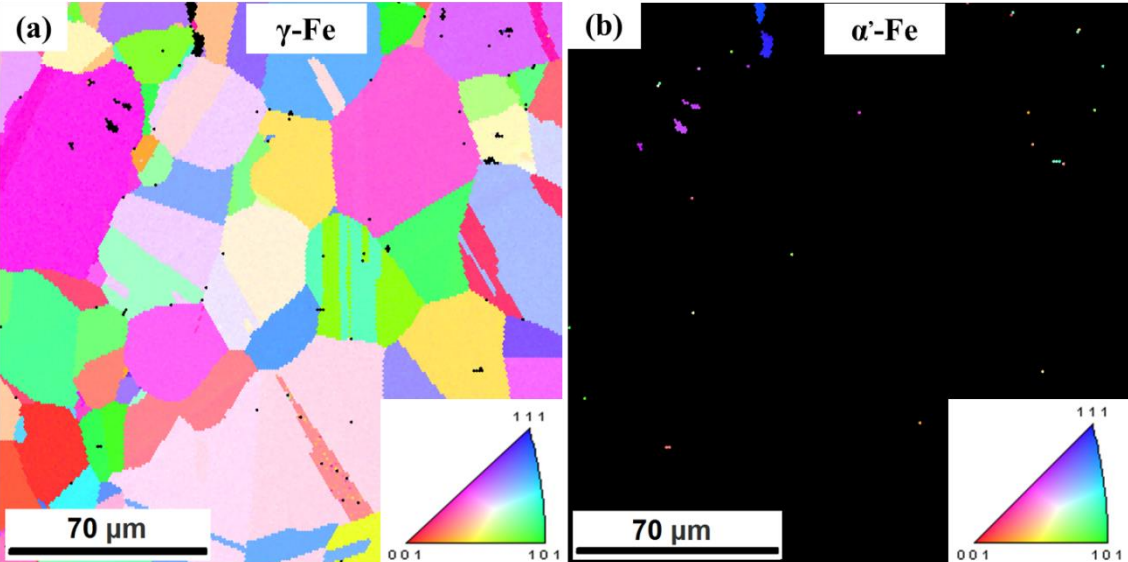


Fig. 2.

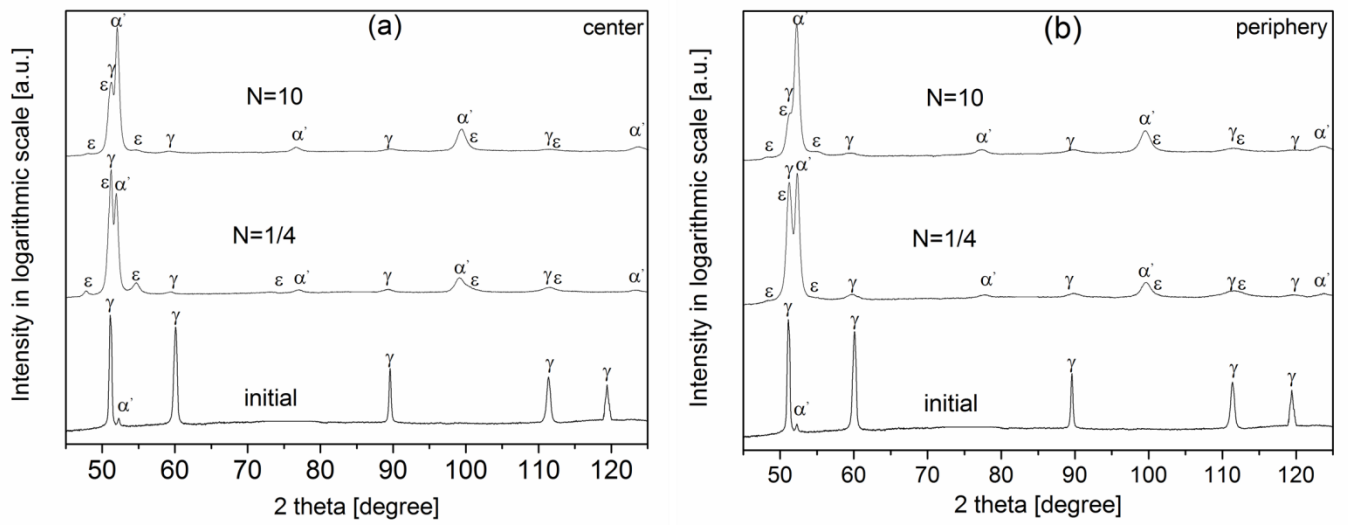


Fig. 3.

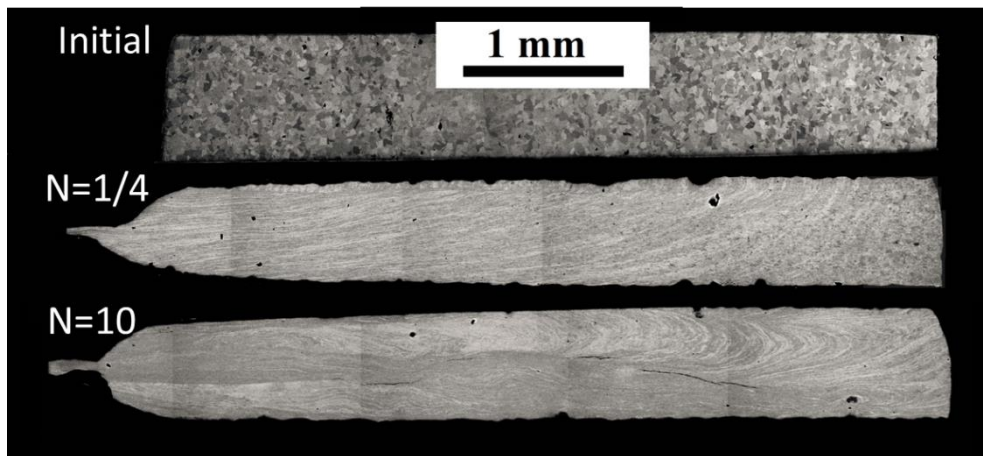


Fig. 4.

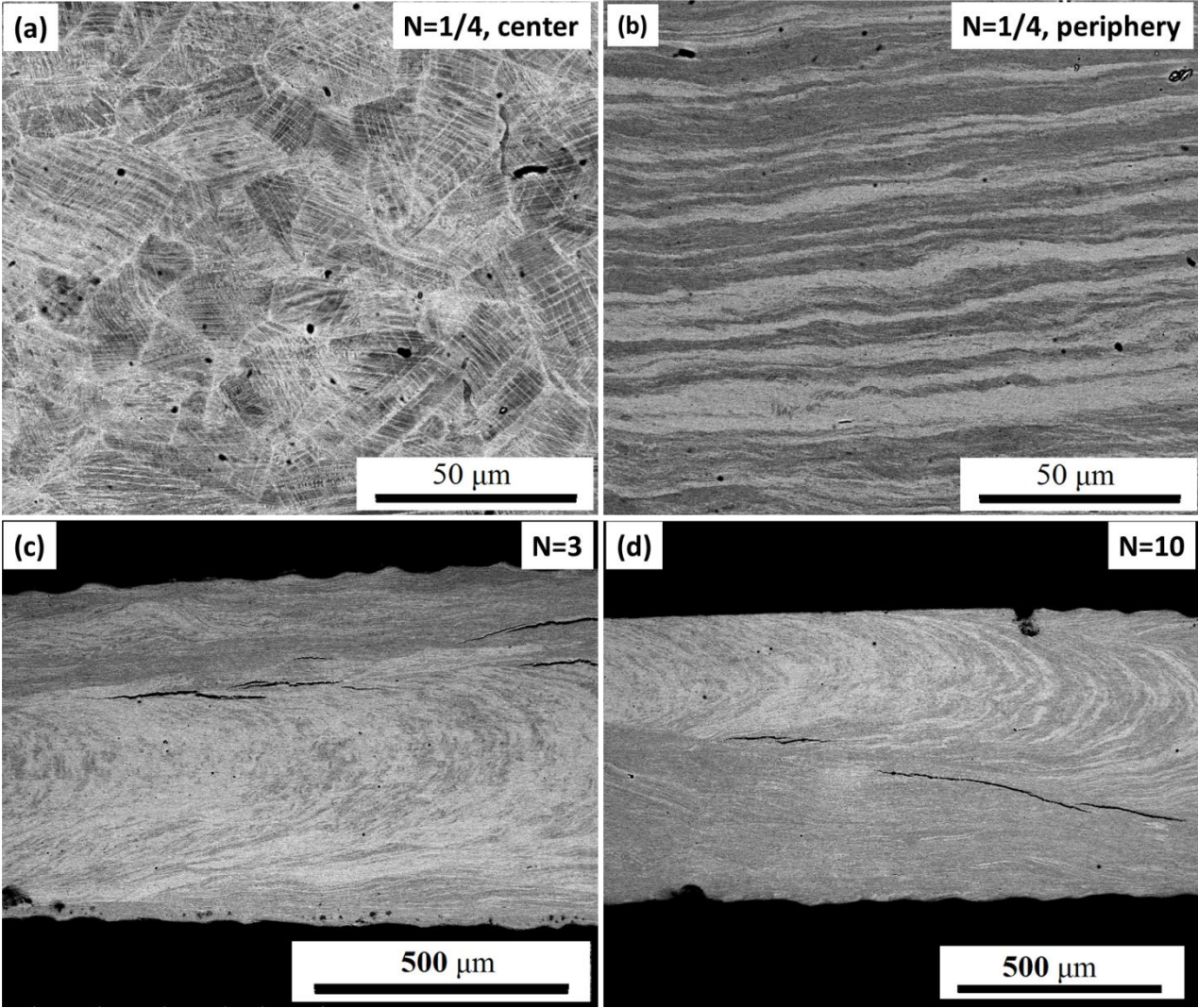


Fig. 5.

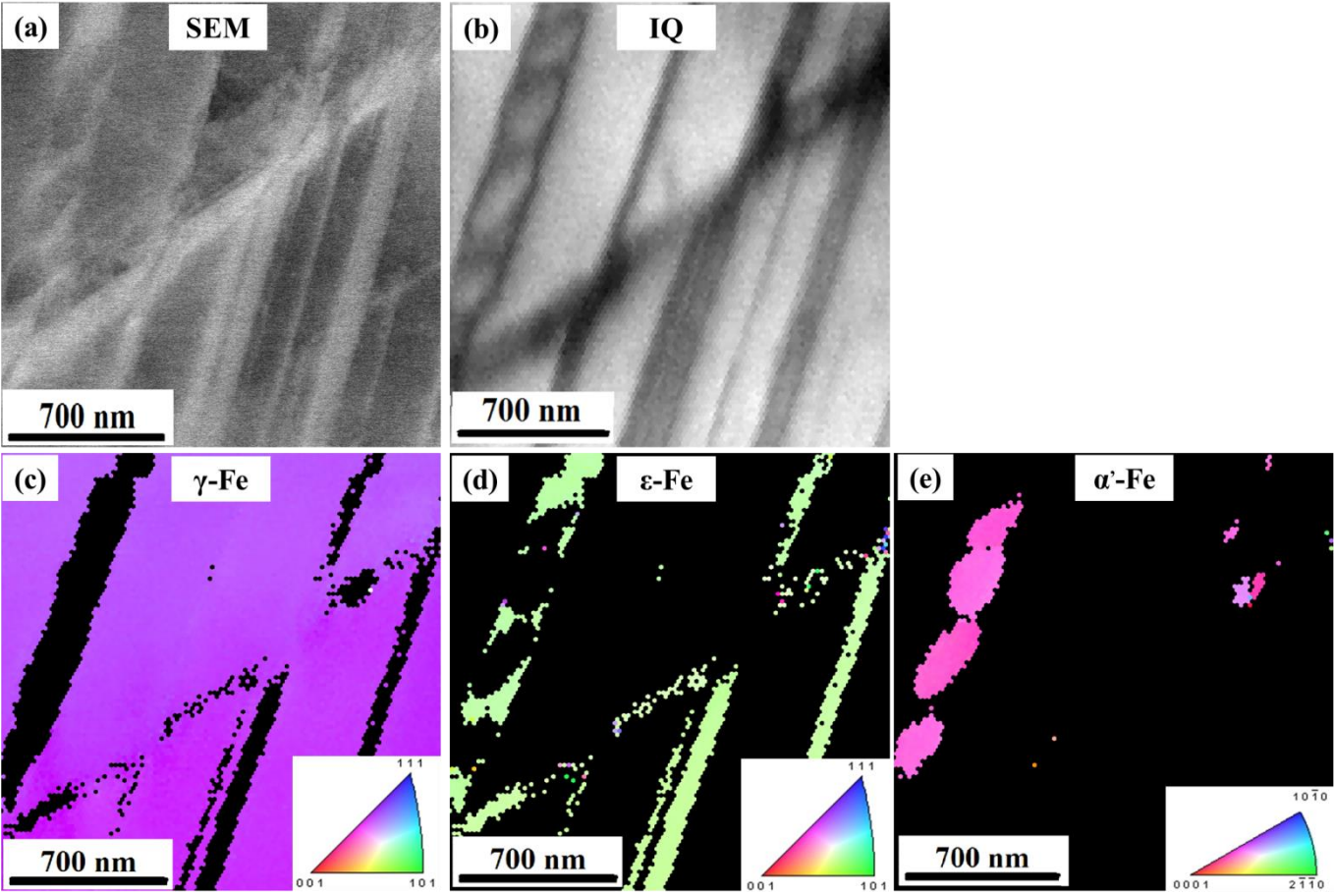


Fig. 6.

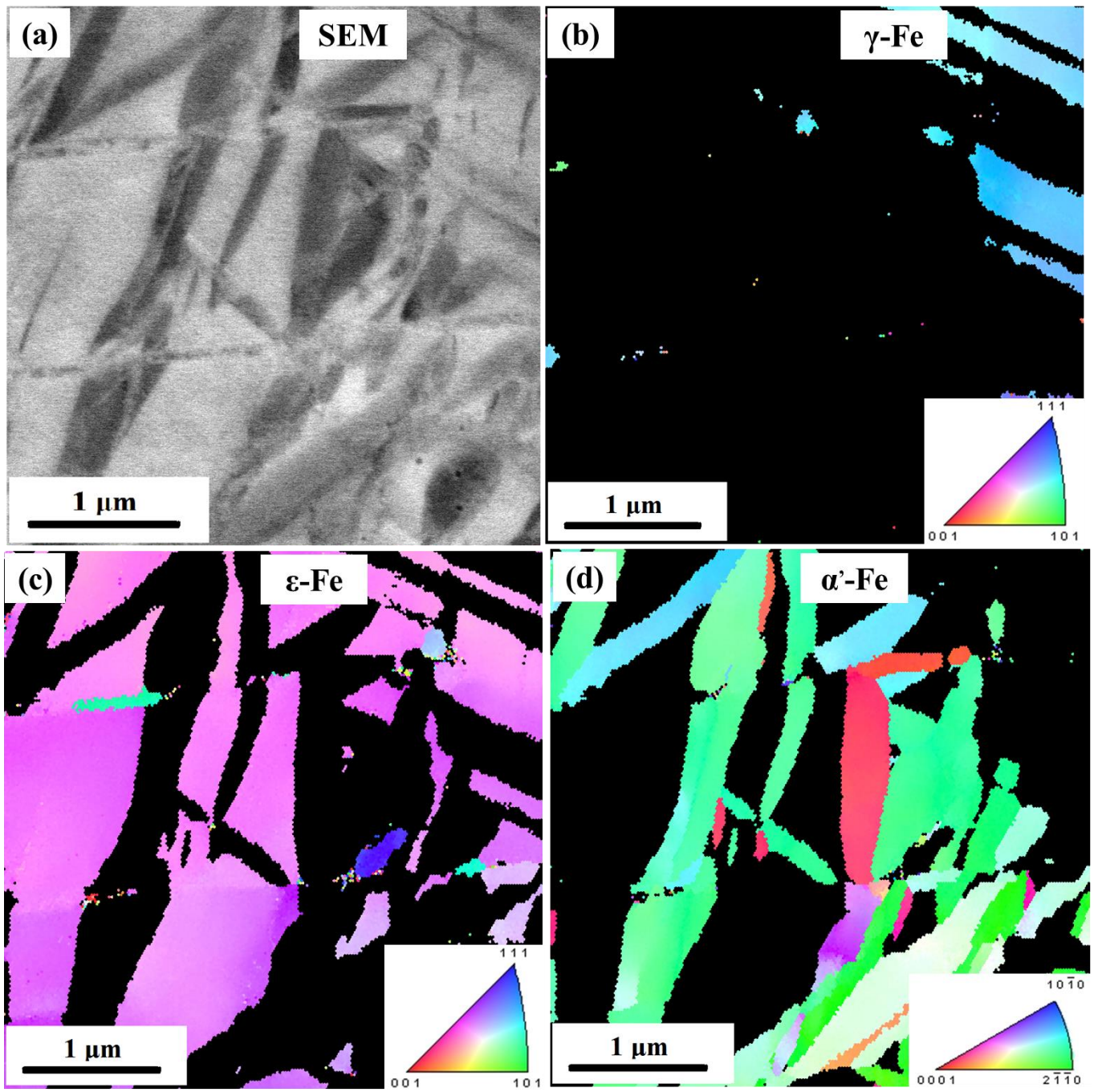


Fig. 7.

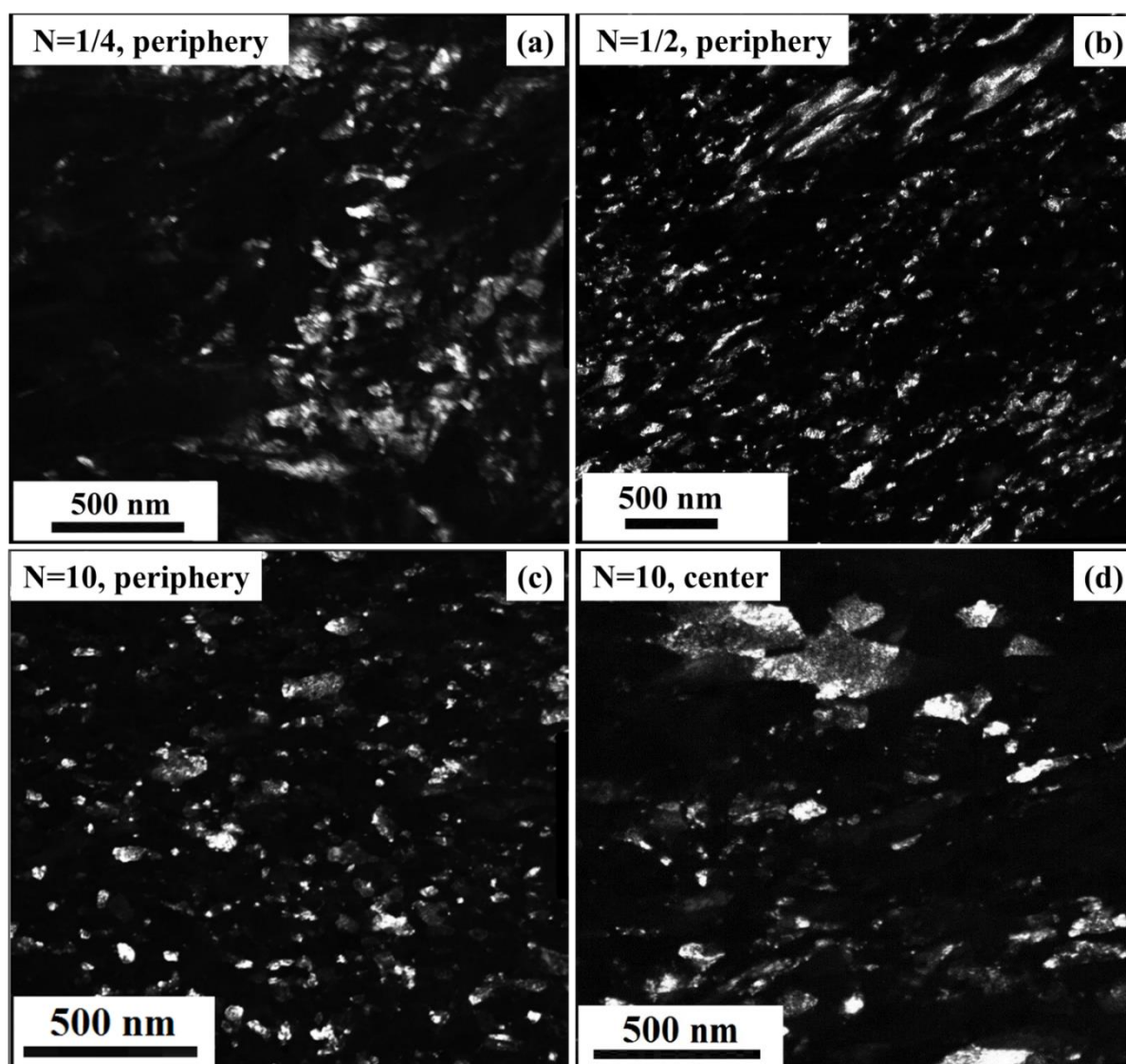


Fig. 8.

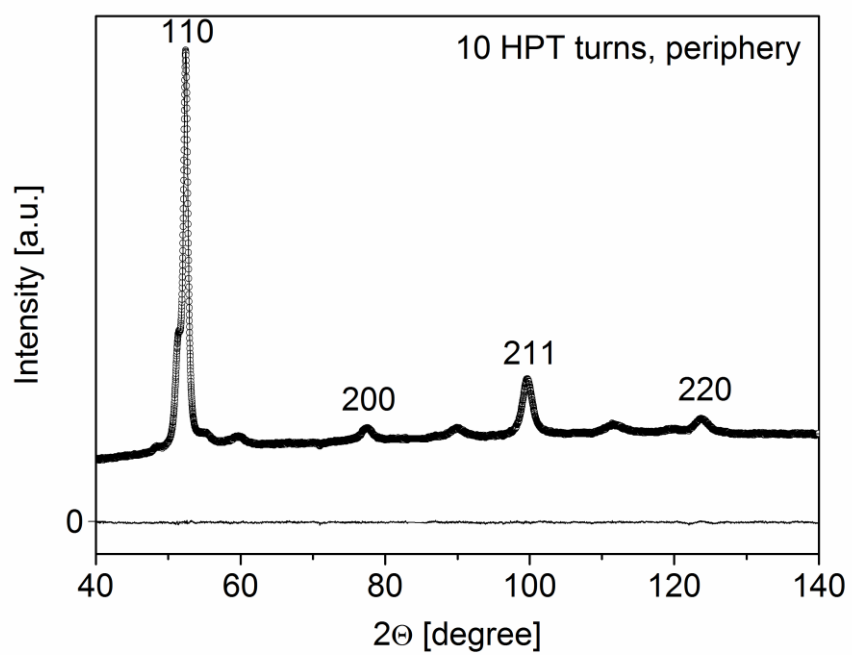


Fig. 9.

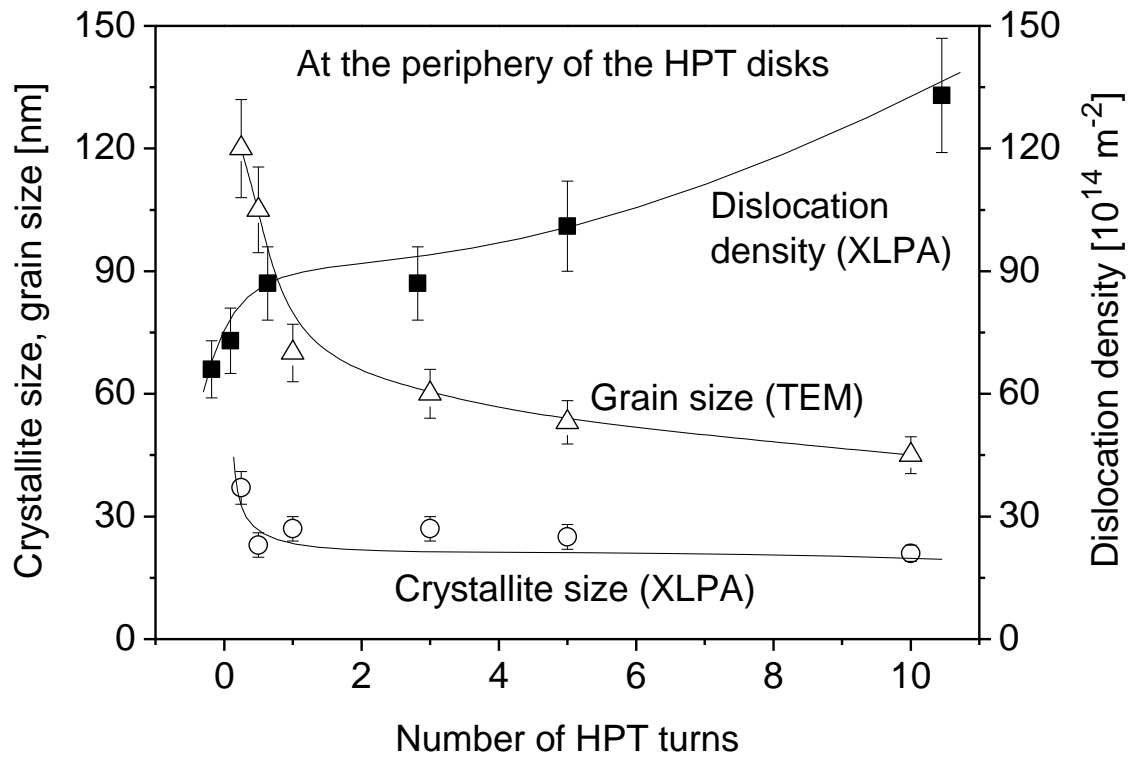


Fig. 10.

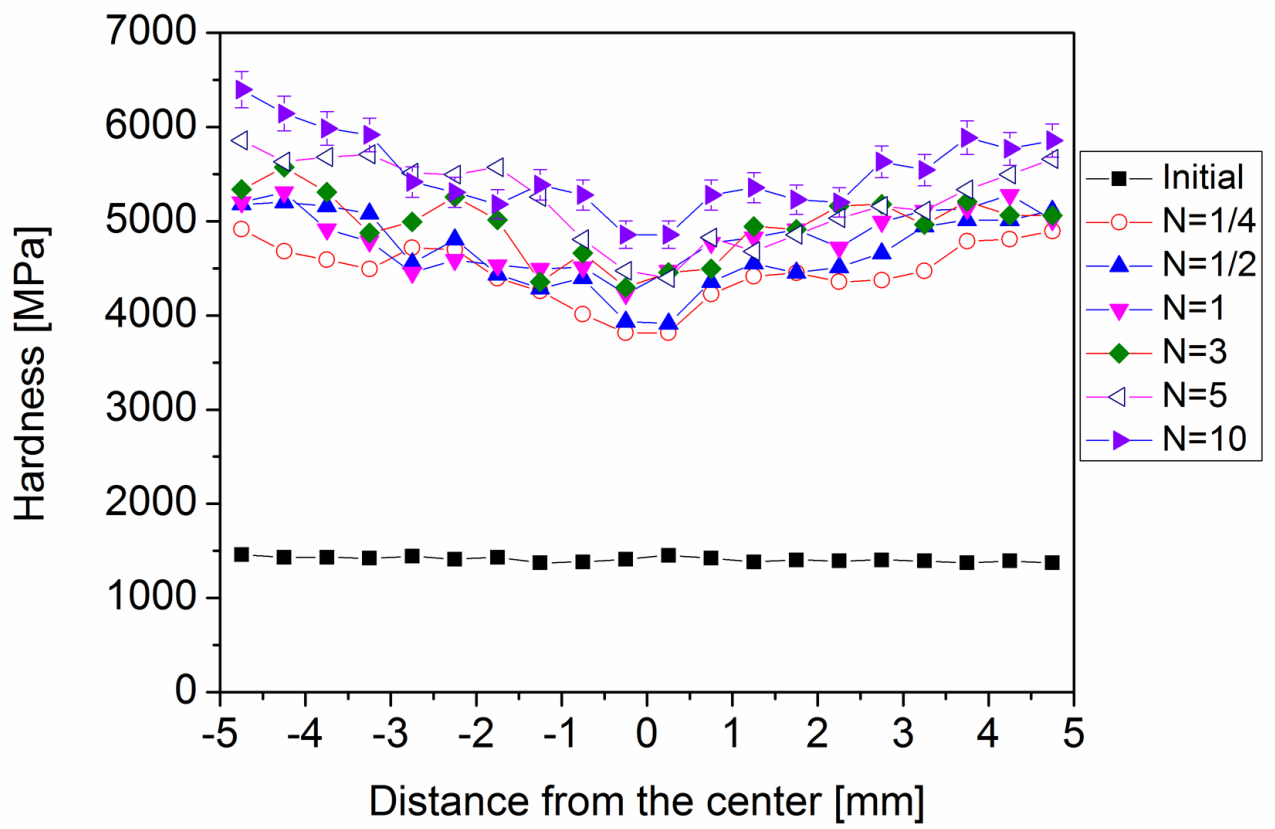


Fig. 11.

